Supporting Information for:

Quantum Dot Nano Thermometers Reveal Heterogeneous Local Thermogenesis in Living Cells.

Jui-Ming Yang[1], Haw Yang[2,3], Liwei Lin[1]

[1]Department of Mechanical Engineering, Berkeley Sensor and Actuator Center, University of California, Berkeley, CA 94720, USA

[2]Department of Chemistry, UC Berkeley, Berkeley, CA 94720,USA

[3]Department of Chemistry, Princeton University, Princeton, NJ 08544, USA

Supporting Information - For Review Only - Not for Publication

Table of Contents

Supplementary Information For Review Only - Not for Publication

1 EXPERIMENT

A small portion of the experimental has been described in the Methods section of the main text. Some of the descriptions are repeated here for completeness.

1.1 Cell culture

The NIH/3T3 murine fibroblast cells (American Type Culture Collection, CRL-1658) were cultured in a glass-bottom Petri dish with high-glucose Dulbecco's modified Eagle medium (DMEM) containing 10% bovine serum with antibiotic mixture. The Ca^{2+}-shock and cold-shock experiments were conducted when cells were at about 40% confluence.

1.2 Quantum dot uptake

For experiments with Ca^{2+}-shock, pH control, confocal imaging, and lamp power control, cells were incubated with 4 µl of 10 nM quantum dot mixture (Invitrogen/Molecular Probes, Qtracker cell labeling kits, Q25021MP; kits used as received) for one hour at 37 °C. After three-time washes with phosphate buffered saline (PBS, pH = 7.4 hereafter if not specified), cells were cultured in fresh DMEM for further experiments. For cold-shock experiments, a layer of 10% type-I collagen (Sigma, C3867) was coated on the glass bottom of the sample Petri dish. Following a one-hour incubation, 200 µl of 10-nM Qtracker quantum dots mixture was added to the partially dried collagen layer. The collagen layer was dried further under ambient conditions for 2 hours. NIH/3T3 cells were then plated on the Petri dishes with the collagen-quantum dot layer and allowed to grow and to uptake quantum dots for 8 hours before imaging.

1.3 Immunofluorescence staining

The procedure for quadruple labeling (internalized quantum dot, mitochondria, nucleus, and F-actin) is briefly outlined below. Following wide-field optical imaging, cells were stained for mitochondria with 100-nM MitoTracker Red CMXRos (Invitrogen / Molecular Probes, M7512) for 30 minutes. Cells were subsequently fixed in 3.7% formaldehyde in PBS for 10 minutes and permeabilized with a solution of 0.1% Triton X-100 for 3 minutes. Cells were then immunostained following standard protocols with 165 nM phallotoxins (Invitrogen / Molecular Probes, O7466) for 20 minutes for F-actin labeling and with 300 nM DAPI (Invitrogen / Molecular Probes, D3571) for 3 minutes for nuclei stain.

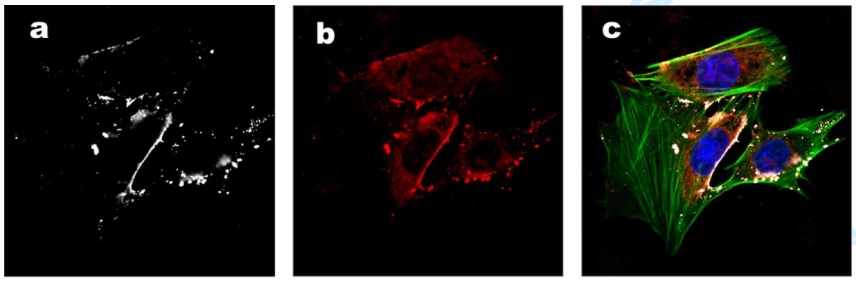

Fig. S1. A confocal fluorescent micrograph of intact cells with quad-labeling with **a.** quantum dots (white), **b.** mitochondria (red), **c.** F-actin (green) and nuclei (blue).

Fig. S1a shows the fluorescence image of quantum dot internalization, presumably in the form of endocytotic vesicles(*1, 2*), and their co-localization with various cellular organelles in NIH/3T3 cells. Fig. S1b and S1c show mitochondria labeling in red, and the composite image with actin filaments labeled in green and

Supporting Information - For Review Only - Not for Publication

nuclei in blue. These images were acquired using a Zeiss 510 META NLO two-photon confocal microscope in the Cancer Research Laboratory Molecular Imaging Center at the University of California, Berkeley.

In addition to mitochondria, another potential heat source is Ca^{2+}-ATPase(*3-6*) which can be clocked by the Ca^{2+}-ATPase thapsigargin(*7*), as has been reported by Suzuki *et al.*(*8*). The intra-cellular distribution and the dynamics of sarcoplasmic reticulum Ca^{2+}-ATPase has recently been reported by Cusimano *et al.*(*9*), whose results indicate that there are significant variations in the Ca^{2+}-ATPase density distribution. Taken together, our data were consistent with the known literature results.

1.4 Apparatus

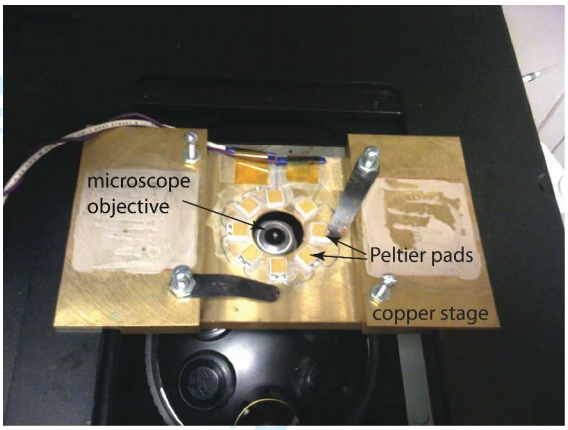

Fig. S2. Photograph of the home-built Peltier temperature control unit and sample mount.

The experimental configuration was schematically shown in main-text Fig. 1a. The Petri dish sample chamber containing a micro thermocouple was mounted on a home-built Peltier temperature control unit, as shown in Fig. S2. The entire platform was secured on an inverted microscope (Olympus, IX-71). A mercury lamp was used as the illumination light source. The excitation light was attenuated and spectrally filtered, and was directed via a dichroic mirror (Chroma, 560dclp) to the microscope objective 20× to focus on the sample. The emission from the cell auto-fluorescence and endocytosed quantum dots was collected by the same microscope objective, channeled through an emission spectral filter, and focused into a spectrograph (Acton Research/Princeton Instruments, SP2150i). The spectrograph was equipped with a 600 groves/mm grating blazed at 500 nm to give a spectral dispersion of 9 nm/mm. The entrance slit width was set to 100 μm, which provided good background rejection with decent spectral resolution, and simultaneously permitted prolonged observation time since some quantum dots may move out of the observation window during experiment. The spectrally resolved light was detected by a CCD camera with single-molecule sensitivity (Roper Scientific, Cascade 512B) running at 16-bit resolution. The camera had an imaging area of 8.2×8.2 mm^2 with 512×512 pixels. Combined with the monochromator dispersion, the conversion factor from pixel to wavelength is 0.144 nm/pixel.

Supporting Information Revised Only for Peer Review Not for Publication

1.5 Image acquisition

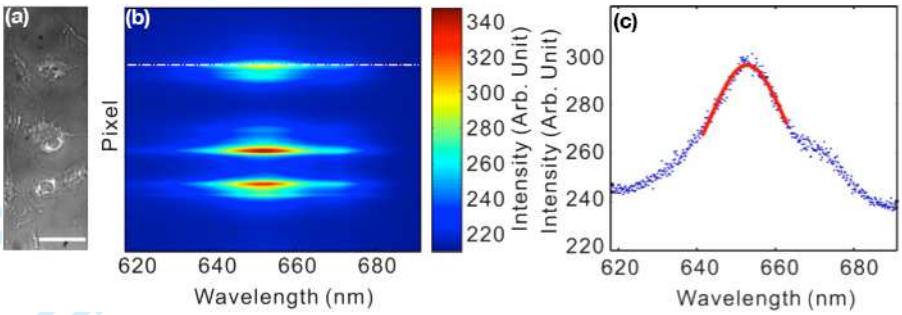

Fig. S3. Position-spectral imaging of quantum dots in cells. **a.** A wide-field image of three cells within the observation window. The scale bar at the bottom right is 15 mm. **b.** Quantum dot spectra along a vertical line in **a** that includes approximately 3 groups of quantum dots. **c.** Spectrum (blue dots) of the quantum dot indicated by the white dashed-dot horizontal line in **b**. A Gaussian fit to the spectrum (red solid line) is also displayed to illustrate how the spectral mean can be recovered.

To locate intracellular quantum dots, the grating of the spectrograph was set to the zeroth order for imaging (Fig. S3a). Once a suitable cell and quantum dot spot was located, the grating was switched to the first order for time-dependent spectroscopic investigation (Fig. S3b). The exposure time of the CCD camera was adjusted in each experiment to visually optimize the image quality. For Ca^{2+}-shock experiments, the exposure time ranged from 400 ms to 700 ms and the time-lapsed images were taken every ~3 s. For cold-shock experiments, the exposure time ranged from 100 ms to 300 ms and the time-lapsed images were taken every 6 s. The precise exposure and delay times were recorded in the raw image files and were included in data analysis. The digitized spectral images were recorded by WinView32 (Roper Scientific) running on a Windows PC and saved to a hard drive for analysis. Fig. S3c illustrates the kind of spectra one would get from this setup. In our data analysis, we used a two-dimensional Gaussian fit to simultaneously analyze the position (the direction along the ordinate in Fig. S3b) and the spectral mean (the abscissa). The previously published wavelength-to-temperature conversion(*10*), 0.105 nm/°C, was used to convert wavelength shift to temperature change.

1.6 Ca^{2+}-shock experiment

Ionomycin calcium salt (Sigma) was used to trigger cellular thermogenesis. Cells containing internalized quantum dots were cultured in the Petri dish under the standard conditions (37 °C and 5% CO_2). Prior to the experiments, the Petri dish sample was equilibrated to room temperature, the same temperature as other chemicals, to prevent sudden temperature change to the sample due to the addition of solutions. The Petri dish was placed on the imaging platform to record quantum dot spectra. For each experiment, 10 µl of 0.05 mM solution containing ionomycin calcium complex was added to the sample, which contained 500 µL of the medium, so that the final Ca^{2+} concentration was ~1 µM.

1.7 Cold-shock experiment

The experimental procedure was largely analogous to the Ca^{2+}-shock experiment. The data acquisition was initiated at the same time when the Peltier cooling was turned on.

2 ANALYSIS

Supporting Information - For Review Only - Not for Publication

2.1 Image analysis

In general, the density of quantum dots was adjusted such that the spots were sparse in a cell. This made the identification and tracking relatively straightforward. Nevertheless, we developed an automated data analysis algorithm in order to minimize subjectivity from manual data process and to let the data lead to unbiased conclusions. The data analysis, including image process and statistical analysis, were carried out using MATLAB version R2009b (Mathworks). For each single cell, the time-dependent quantum dot spectral evolution was analyzed sequentially by the steps described below.

2.1.1 Detection and localization of quantum dot spots in position-spectrum images

The high frequency noise in a raw image, $\mathbf{Img}_{\text{raw}}$, was first removed by wavelet de-noising using the coif2 wavelet to the 4$^{\text{th}}$ level (wavedec2(), ddencmp(), wdencmp()). The de-noised image was designated as $\mathbf{Img}_{\text{denoise}}$. The mean and standard deviation of pixel counts for the de-noised image, S_{denoise} and σ_{denoise}, respectively, were then calculated. The background level was estimated using $B_{\text{denoise}} \equiv S_{\text{denoise}} + 1.95\sigma_{\text{denoise}}$. The background was then removed by $\mathbf{Img}_{\text{dn\_nobkg}} = \mathbf{Img}_{\text{denoise}} - B_{\text{denoise}}$, where pixels with a negative count were set to 0. The automated spot-finding algorithm shipped with MATLAB was used to detect and locate quantum dot spots (strel(), imerode(), imreconstruct(), imdilate(), imreconstruct(), imcomplement(), imregionalmax(), regionprops()). The computer-localized spot coordinates were used as the initial guess for subsequent c^2-fits to two-dimensional Gaussian centroids. Note that the raw image data, $\mathbf{Img}_{\text{raw}}$, was used in the fitting; the initial de-noising steps were only for spot finding. The non-linear fitting was carried out using the Levenberg-Marquardt algorithm (*11, 12*) (lsqnonlin()). For the *i*-th spot in the image of time index *t*, the fitting gave the mean position $\hat{x}_{i,t}$, and the spread of the quantum dot spot on the image $\hat{\sigma}(x_{i,t})$ as the width of the position Gaussian. The uncertainty of the position, $\delta(\hat{x}_{i,t})$, was estimated by calculating the covariance matrix of the c^2 merit function, which in turn gave the standard deviation of the $\hat{x}_{i,t}$ fit (*13*). The fitting also generated analogous parameters along the wavelength coordinate to give, $\hat{\lambda}_{i,t}$, $\delta(\hat{\lambda}_{i,t})$, and $\hat{\sigma}(\lambda_{i,t})$. These parameters from fitting were used in subsequent data analysis. The image processing for the cell shown in main-text Fig. 1b and Fig. 2 is illustrated in Fig. S4.

Supporting Information - For Review Only - Not for Publication

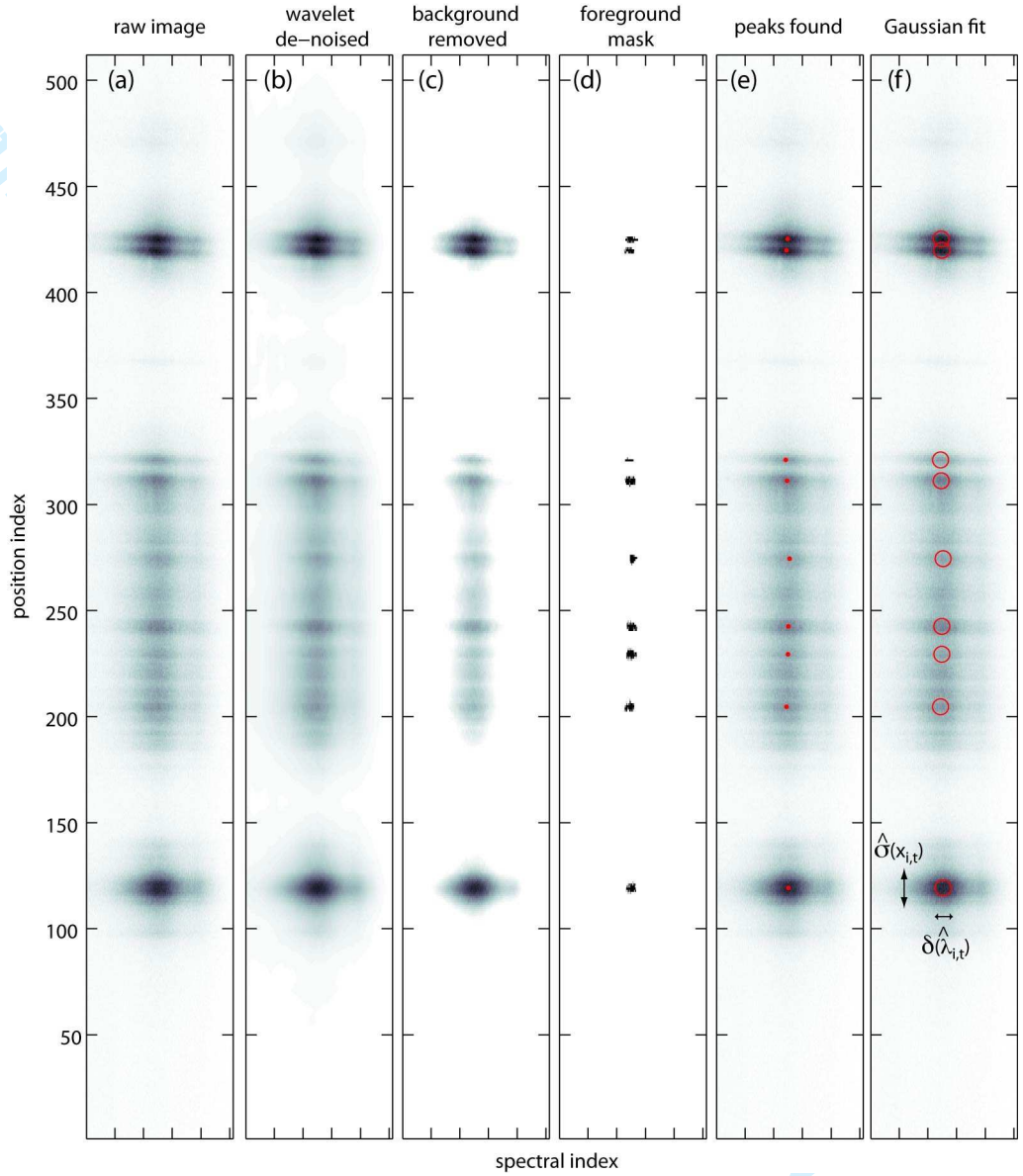

Fig. S4. Illustration of the image processing using the first frame of the data set in Fig. 2 in the main text. (a) Raw position-spectrum image, $\mathbf{Img}_{\text{raw}}$. (b) Wavelet de-noised image, $\mathbf{Img}_{\text{denoise}}$. (c) Background-removed image, $\mathbf{Img}_{\text{dn\_nobkg}}$. (d) Spots located using MATLAB built-in image process functions. (e) Overlay of the spot mast with the raw image, in which the spots were used as initial guess for Gaussian fits. (f) Gaussian fit results, where the quantum dot spot position spread $\hat{\sigma}(x_{i,t})$ and the uncertainty in spectral mean (note: not the spectral spread) $\delta(\hat{\lambda}_{i,t})$ are indicated by arrows.

Supporting Information
Not for Publication

Supporting Information - For Review Only - Not for Publication

2.1.2 Classification of quantum dot positions

Some of the quantum dot spots drifted during the experiment. In order to follow the temperature evolution for a specific spot, it was necessary to correlate quantum dot positions in different time frames. Since there was no *a priori* knowledge of the manner by which the quantum dot spots should move—the diffusion model was certainly inappropriate—a data-driven approach was needed. The problem of correlating spots between frames was isomorphic to the classification problem in applied statistics (*14*). We employed the idea put forward by Matusita in *circa* 1950 (*15-18*), by which one could define a distance measure between the two distribution functions P and Q (also called the Hellinger distance(*19*)),

$$\|P-Q\| \equiv \sqrt{\sum_j \left(\sqrt{p_j}-\sqrt{q_j}\right)^2}, \tag{S1}$$

where j runs through all indices. As shown by Matusita(*20-23*), the Hellinger distance has a nice relationship to the c^2 statistics:

$$\Pr\left(\|F-S_n\| > \eta\right) \approx \Pr\left(\chi^2_{(k-1)} \geq 4n\eta^2\right), \tag{S2}$$

where F denotes the distribution of the discrete random variable under consideration, S_n the empirical distribution for n observations on the variable, k the number of values the variable takes on, and $\chi^2_{(k-1)}$ a c^2 distribution with (k-1) degrees of freedom. Eq. (S2) served as the test statistic for deciding whether two quantum dot spots were correlated.

In the present application, P and Q were the two Gaussian distributions from the fitting, $\mathcal{N}(\hat{x}_{i,t}, \hat{\sigma}(x_{i,t}))$ and $\mathcal{N}(\hat{x}_{k,t+s}, \hat{\sigma}(x_{k,t+s}))$, representing potentially correlated quantum dot spots at the t-th and the $(t+s)$-th frames. This allowed for correlating frames that are separated by more than one time increment to address the missing frame problem. Here, a critical value of $\eta = 1.2$ was used, by which two spots with a Hellinger distance greater than 1.2 were deemed uncorrelated. The correlated quantum dot spots were strung together as the initial guess for subsequent spot tracking and cross-validation.

2.1.3 Cross validation of model-free quantum dot spot tracking

To manage the complication that resulted from missing frames and misclassification, we developed a particle-tracking algorithm that did not require a model for the particle movement. It incorporated the ideas of interpolation and extrapolation (*24*), as well as multi-frame reconstruction, trajectory fusion, and cross validation (*25*). The algorithmic flow followed the basic outline described by Li *et al.* (*25*) but, instead of using a known dynamics model, a 3rd-order B-spline fit was used to obtain a smooth representation of the quantum dot position. That is, an implicit assumption of this treatment was that the quantum dot position was a smooth function of time. Each position point was cross validated with respect to the spline fit to ensure that it belonged to the empirical trend as described by the spline. In the point-by-point cross validation, Eq. (S2) was used as the criterion for acceptance or rejection.

The next step was to examine whether the two trajectories could be joined together. Consider two non-overlapping trajectories, **traj1** and **traj2**. For the sake of discussion, let us assume that **traj1** proceeds **traj2**. To examine whether these two trajectories could be joined, **traj1** was extrapolated to the first time point of **traj2** using B-spline extrapolation. Then Eq. (S2) was used to test if the first point of **traj2** belonged to the **traj1** extrapolation. The procedure was repeated to examine the last time point of **traj1** against extrapolation of **traj2**. **traj1** and **traj2** were considered to be the same trajectory if and only if both tests were successful.

Finally, trajectories that were shorter than 10 time points, or did not start in the first 10 time points were rejected. This was because the temperature progression as measured by quantum dots only reported the temperature relative to the first time point at t = 0. A representative result is shown in Fig. S5.

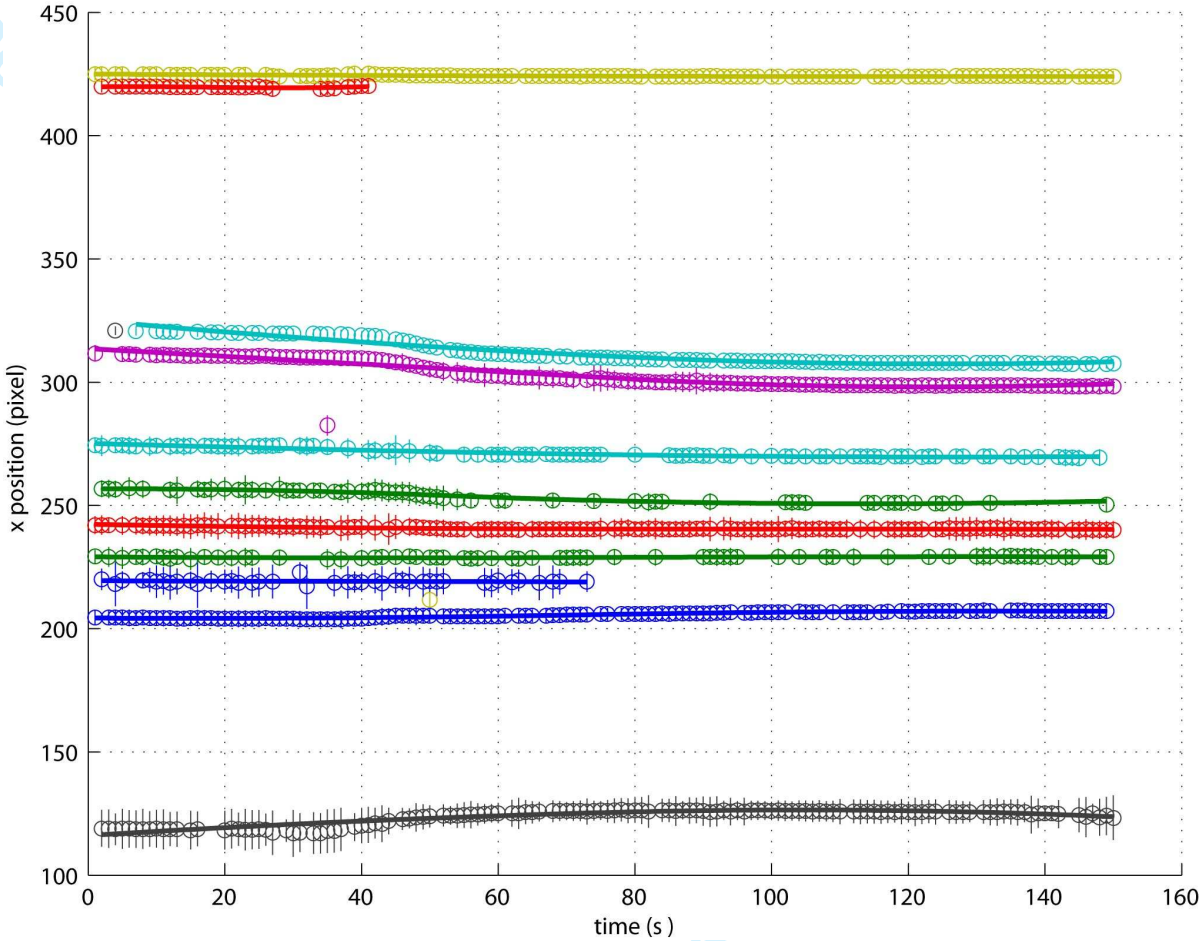

Fig. S5. Representative image-based tracking. The position uncertainties associated with each data point (vertical bars) are position spread, $\hat{\sigma}(x_{i,t})$, from Gaussian fit. Quantum dot trajectories are designated with different color. Solid lines are spline fits to the time-dependent positions and shown here as eye guides.

2.2 Statistical analysis

In this section, we describe the procedures involved in presenting the figures as well as the statements made in the main text.

2.2.1 Error bars in position-time and temperature shift-time plots

Main-text Fig. 2b, Fig. 2d, Fig. 3a, Fig. 3b, and Fig. 3c contain plots in which error bars were represented by shades of temperature color. The plots were constructed this way to help visualize and assess the temperature measurements and their correlation with various parameters such as time and position. In the position-time plots, Fig. 2b and Fig. 3a, the Gaussian widths used in constructing them were the size of the quantum dot spot, $\hat{\sigma}(x_{i,t})$, from the position fitting (cf. section 2.1.1). In the temperature-time plots, Fig. 2d, Fig. 3b, and Fig. 3c, the Gaussian widths were the uncertainties in the spectral mean $\delta(\hat{\lambda}_{i,t})$ converted to uncertainties in temperature $\delta(\Delta T_{i,t}) = \delta(\hat{\lambda}_{i,t}) / 0.105$ (nm/°C).

Supporting Only - Not for Publication

2.2.2 Cell-by-cell temperature change in Ca^{2+}-shock experiment

The data presented in the inset of Fig. 2c were calculated as follows. For each cell, the measured temperature shifts for the *i*-th quantum dot trajectory, $\{\Delta T_{i,t}\}$, were divided into two sections, those that were before Ca^{2+} addition ($0\text{ s} < t \le 100\text{ s}$) and those that were after calcium shock ($350\text{ s} < t \le 450\text{ s}$). Collecting all the measurements from the same cell, we had data sets $\{\Delta T_{0<t\le100}\}$ and $\{\Delta T_{350<t\le450}\}$. The question was whether, statistically, the average of $\{\Delta T_{350<t\le450}\}$ was greater than, equal to, or less than that of $\{\Delta T_{0<t\le100}\}$. To answer this question, we performed a two-sided *t*-test by Welch(*26*), which allowed unequal variances of the two populations under consideration. The tests were carried out with 95% confidence, or 5% type-I error, for the difference in the population means.

Not all the cells showed a temperature rise in this series of experiments. This observation could be understood by considering three contributing scenarios. It was possible that cell-to-cell variations in cellular physiology were such that each cell might respond to Ca^{2+} shock differently. While some responded with greater heat generation, some might respond with little heat generation. The second possible reason was that the quantum dots were internalized and distributed inside the cell in a non-specific way. It was therefore likely that for some cells, the quantum dots settled to regions that were far away from the local heating source such that the mean temperature change was negligible. The third possible reason had to do with the quantum dot movement during experiment. Quantum dot drifts along the position axis in a position-spectrum image (cf. Fig. S4, S5) were corrected by image-based tracking. Drifts along the spectral axis, however, could not be completely rectified and thus could contribute to appreciable uncertainties. This scenario will be discussed in more detail in section 2.3 below.

2.2.3 Broader temperature progression distribution in live cells.

For Fig. 2c in the main text, the temperature measurements from all 31 cells, $\{\Delta T_{0<t\le100}\}$ and $\{\Delta T_{350<t\le450}\}$, separate histograms were constructed and compared. The bin width for the histograms was determined using the Freedman-Diaconis rule (*27*) for optimal width. This was important to remove potential subjectivity in choosing the bin width, which in turn could lead to a biased view of the data.

To quantitatively compare the two data sets, $\{\Delta T_{0<t\le100}\}$ and $\{\Delta T_{350<t\le450}\}$, Welch's *t*-test (*26*) was used to test whether the mean of $\{\Delta T_{350<t\le450}\}$ was greater than that of $\{\Delta T_{0<t\le100}\}$. With 95% confidence, the test indicated that there was an average temperature increase after calcium shock. We next compared the widths. Since the distributions in the temperature shift were not necessarily Gaussian, Levene's test (*28*) was used to examine whether the width of $\{\Delta T_{350<t\le450}\}$ was greater than that of $\{\Delta T_{0<t\le100}\}$. The test concluded that the width of local temperature distribution after calcium shock was indeed greater than the temperature distribution before calcium shock. The statement could be made with a *p*-value of 2.6×10^{-15}.

Similarly, for Fig. 3d in the main text, one could make the statement that the width of live cells was greater than that of dead cells with a *p*-value of 2.5×10^{-10}. The quantitative statistical analyses of the experimentally measured temperature progression distribution lead us to conclude that in live cells, the local temperature response was heterogeneous.

2.3 Error analysis

The absolute temperature measurement requires a homogeneous spectral response from every single quantum dot. Given the extent of spectral heterogeneity in the commercially available quantum dots (*10, 29*), this goal is not yet achievable. Further innovation in the fabrication of high quality quantum dots will therefore significantly advance the field. On the other hand, the *relative* temperature shift measured from a collection of quantum dots has been shown to be reliable (*10*). The remainder of the discussion therefore focuses on the error analysis of relative temperature measurements.

Supporting Information - For Review Only - Not for Publication

Supporting Information - For Review Only - Not for Publication

2.3.1 Instrument drifts

Drifts in the microscope and monochromator might occur during the 15-min measurement time. The drift along the position axis could be compensated for by image-based tracking (cf. Fig. S4, Fig. S5 and section 2.1). The drift along the wavelength axis, however, could not be completely compensated by tracking, contributing to uncertainties in temperature measurements. The maximum amount of spectral shift due to quantum dot move along the spectral axis could be estimated from the width of the monochromator entrance slit, $100\ \mu$m, by $100\ (\mu\text{m}) / 16\ (\mu\text{m/pixel}) = 6.25$ pixel $= 0.9$ nm $= 8.57\ ^\circ$C. To estimate the temperature uncertainties due to instrument drift under experimental conditions, we assumed that the probabilities of drifting along the position and the spectral axes were the comparable (details of the model is described in the next section, 2.3.2). Under this assumption, one had,

$$\delta(\Delta\lambda)_{\text{instrument drift}} \approx 0.144 \times \delta(\Delta x)_{\text{instrument drift}}, \qquad \text{(S3)}$$

where $\delta(\Delta x)_{\text{instrument drift}}$ was in units of pixel and the conversion factor of 0.144 nm/pixel from pixel to wavelength was used. The position drifts in the fixed-cell Ca^{2+}-shock experiment were used to calculate $\delta(\Delta x)_{\text{instrument drift}}$. Specifically, $\delta(\Delta x)_{\text{instrument drift}}$ was calculated as the standard deviation of the data set, $\{\Delta x_{i,t}\}$, with $\Delta x_{i,t} \equiv x_{i,t} - x_{i,t=0}$ and i being the quantum trajectory index. An analysis of the fixed-cell Ca^{2+}-shock data gave $\delta(\Delta x)_{\text{instrument drift}} = 0.450$ pixel. This corresponded to $\delta(\Delta\lambda)_{\text{instrument drift}} = 0.0648$ nm and $\delta(\Delta T)_{\text{instrument drift}} = 0.617$ °C, where the conversion from wavelength to temperature was 0.105 nm/°C(*10*).

2.3.2 Quantum dot movements

In the live-cell Ca^{2+}-shock experiment, cells became highly agitated following the Ca^{2+}-shock treatment, causing the quantum dots spots to move more significantly. Furthermore, cold-shock experiments for both the live and fixed cells, the quantum dot spots could move because of the cooling-induced morphology change in the cell. The latter case could be understood by considering cells as soft materials so that cold-shock induced quantum dot movements were related to cold-induced shrinkage, for example.

In all cases, one expected different extent of quantum dot movements under different experimental conditions, *e.g.*, Ca^{2+} shock or cold shock. Therefore, it was necessary to devise a way to characterize temperature measurement uncertainties resulting from quantum dot movements. To this end, we considered a simple model that contained the essential elements of the experiment. As depicted in Fig. S6a, the quantum dot spot was projected to the camera chip where each sensing element (pixel) is shown as a gray grid point. Quantum dot movements along the position axis (denoted x) could be relatively extensive but could be followed by the image-tracking algorithm (section 2.1). On the other hand, movements along the spectrum axis (denoted y) would be curtailed by the observation window as defined by the entrance slit. The slit width in the experiment was $100\ \mu$m, corresponding to $100/16 = 6.25$ pixels. The model assumed that the quantum dot spot had equal probability to move along the position or the spectrum axes. Thus, the two-dimensional distribution of quantum dot spot displacement relative to its t = 0 position could be estimated by making a two-dimensional revolution using the distribution measured from tracking along the x direction. The two-dimensional position distribution is depicted by the orange gradient in the figure. The trajectory would terminate if the quantum dot spot moved along the spectrum axis beyond the observation window. Therefore, on the pixel basis, the observed displacement along the spectrum (y) axis would be much reduced relative to the displacements along the position (x) axis, and could be estimated by calculating the standard deviation of position displacements that were $|\Delta x| \le \frac{6.25}{2} = 3.125$ pixels.

Fig. S6b shows the position displacement distribution in Ca^{2+}-shock experiment including all 31 cells. The displacements were calculated from trajectory time points between 350 – 450 sec relative to the mean position, averaged over the first 30 sec. The vertical dashed lines indicate the entrance slit width of the monochromator; displacements along the spectrum axis beyond these boundaries would not be observable. The

standard deviation along the spectrum axis was calculated to be $\sigma(\Delta x) = 1.25$ pixels $= 0.180$ nm $= 1.71$ °C. A more complete characterization is summarized in Table S1, in which the Ca^{2+}-shock experiment was further divided to four categories: cells with average temperature increase ($\Delta T > 0$) before Ca^{2+}-shock (-Ca^{2+}, 30–70 sec in the trajectory) and after Ca^{2+}-shock (-Ca^{2+}, 350–450 sec in the trajectory), cells with no temperature change ($\Delta T = 0$, 350–450 sec in the trajectory), and cells with average temperature decrease ($\Delta T < 0$, 350–450 sec in the trajectory).

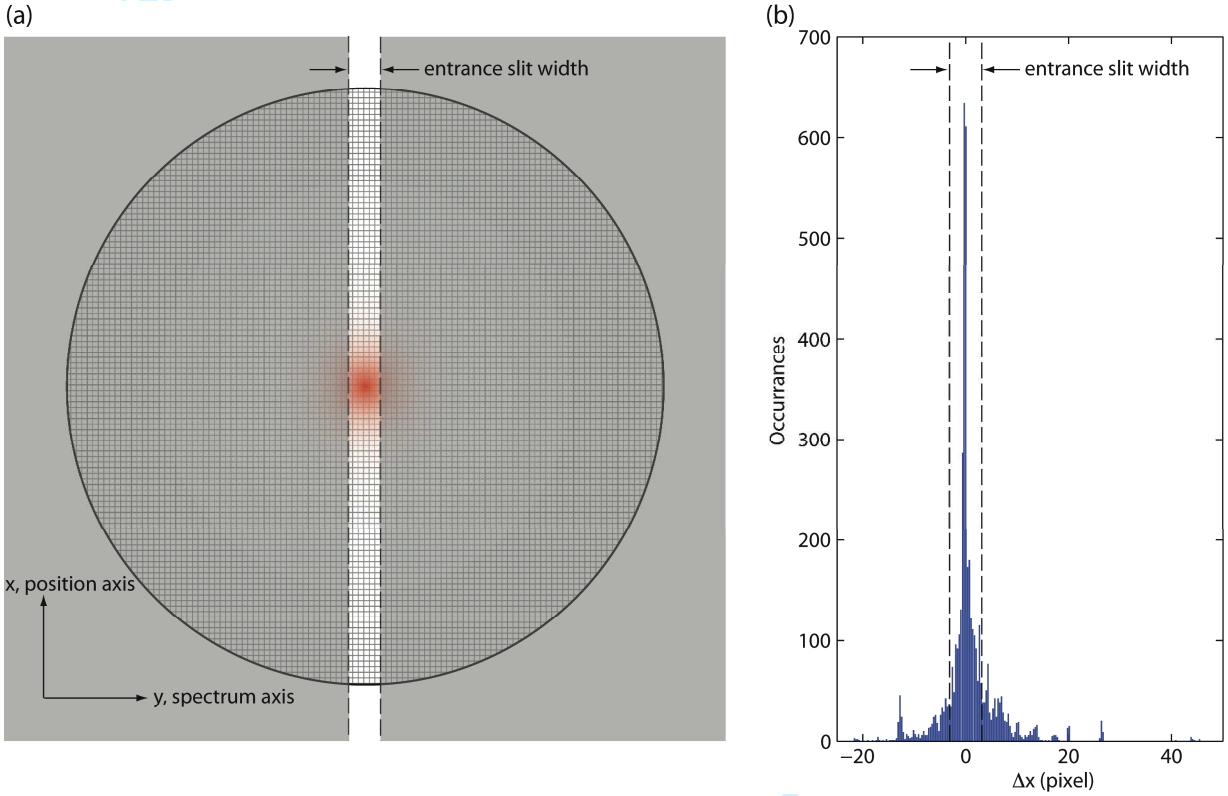

Fig. S6. *In situ* estimate of uncertainties of spectral shift due to quantum dot movements. (a) A simple model containing the essential elements of the experiment. The gray meshes represent imaging pixel matrix. The orange gradient illustrates the two-dimensional displacement distribution of the quantum dot spot. (b) Position displacement histogram measured from Ca^{2+}-shock experiments. The vertical dashed-lines are the monochromator entrance slit. The distribution within the confines of the entrance slit was used to estimate spectral measurement uncertainties due to quantum dot spot movements.

2.3.3 Fitting uncertainties

The quantum dot spots in each position-spectrum image were fitted using a two-dimensional Gaussian function,

$$g(x,y) = A\exp\left[-\frac{1}{2}\left(\frac{x-x_{i,t}}{\sigma(x_{i,t})}\right)^2\right]\exp\left[-\frac{1}{2}\left(\frac{y-y_{i,t}}{\sigma(y_{i,t})}\right)^2\right], \quad \text{(S4)}$$

where A was the brightness of the spot, $x_{i,t}$ the true position, $\sigma(x_{i,t})$ the spread of the quantum dot spot, $y_{i,t}$ the spectral mean in units of pixel, and $\sigma(y_{i,t})$ the spectral width. The fitting was done by minimizing the least-squared error,

Submitting
Copyright for Publication

$$\mathrm{L}^2 = \sum_{r,s} \left(\mathrm{Img}_{r,s} - g\left(x_r, y_s\right) \right)^2 , \tag{S5}$$

where $\mathrm{Img}_{r,s}$ was the raw image pixel intensity at (x_r, y_s). The uncertainties in the fitting were estimated following the procedures outlined in Ref. (*13*). Specifically, we computed the curvature matrix $\underline{\underline{\alpha}}$, whose matrix elements were

$$\alpha_{k,l} = \frac{1}{2} \frac{\partial^2 \chi^2}{\partial a_k \partial a_l}, \tag{S6}$$

where a_k or a_l were fitting parameters A, $x_{i,t}$, $\sigma(x_{i,t})$, $y_{i,t}$, or $\sigma(y_{i,t})$. The partial derivative was computed by,

$$\frac{\partial^2 \chi^2}{\partial a_k \partial a_l} = 2 \sum_{r,s} \frac{1}{\sigma_{r,s}^2} \left[\frac{\partial g(x_r, y_s | \underline{\hat{a}})}{\partial a_k} \frac{\partial g(x_r, y_s | \underline{\hat{a}})}{\partial a_l} - \left(\mathrm{Img}_{r,s} - g(x_r, y_s | \underline{\hat{a}}) \right) \frac{\partial^2 g(x_r, y_s | \underline{\hat{a}})}{\partial a_k \partial a_l} \right], \tag{S7}$$

where $\sigma_{r,s}^2$ was the variance of pixel $\mathrm{Img}_{r,s}$ and was approximated by the intensity assuming Poisson noise and $\underline{\hat{a}} \equiv \left(\hat{A}, \hat{x}_{i,t}, \hat{\sigma}(x_{i,t}), \hat{y}_{i,t}, \hat{\sigma}(y_{i,t}) \right)$ was the vector of optimized parameters. The covariance matrix was then computed by

$$\underline{\underline{C}} = \underline{\underline{\alpha}}^{-1}. \tag{S8}$$

Therefore, the uncertainties associated with the fitting process were estimated by, for example,

$$\delta \hat{y}_{i,t} = \sqrt{C_{y_{i,t}, y_{i,t}}} . \tag{S9}$$

The uncertainties are summarized in Table S1.

2.3.4 The observed broadening in Ca^{2+}-shock experiment was not due to uncertainties in measurement.

As mentioned earlier, the uncertainties in determining the quantum dot spectral mean were attributed to three major sources; they were instrument drift, quantum dot movement, and fitting errors. Assuming that these sources contributed to uncertainties independently, the apparent width in the distribution of temperature shift reads,

$$\begin{aligned} \left[\sigma(\Delta T)_{\text{apparent}} \right]^2 \approx & \left[\sigma(\Delta T)_{\text{best estimate}} \right]^2 \\ & + \left[\delta(\Delta T)_{\text{instrument drift}} \right]^2 + \left[\delta(\Delta T)_{\text{quantum dot move}} \right]^2 + \left[\delta(\Delta T)_{\text{fitting error}} \right]^2 . \end{aligned} \tag{S10}$$

In main text Fig. 2c, the apparent widths of the temperature shift distributions before and after calcium shock were $\hat{\sigma}\left(\Delta T^{\text{Ca}^{2+}\text{ shock}}_{\text{before Ca}^{2+}\text{ shock}} \right)_{\text{apparent}} = 1.59\ ^\circ\text{C}$ and $\hat{\sigma}\left(\Delta T^{\text{Ca}^{2+}\text{ shock}}_{\text{after Ca}^{2+}\text{ shock}} \right)_{\text{apparent}} = 2.87\ ^\circ\text{C}$, respectively. Using the error estimations discussed in sections 2.3.1, 2.3.2, and 2.3.3 (summarized in Table S1), we were able to derive the distribution widths after removing the major uncertainty contributions, $\hat{\sigma}\left(\Delta T^{\text{Ca}^{2+}\text{ shock}}_{\text{before Ca}^{2+}\text{ shock}} \right)_{\text{best estimate}} = 1.10\ ^\circ\text{C}$ and $\hat{\sigma}\left(\Delta T^{\text{Ca}^{2+}\text{ shock}}_{\text{after Ca}^{2+}\text{ shock}} \right)_{\text{best estimate}} = 1.90\ ^\circ\text{C}$, where the residual widths, $\hat{\sigma}_{\text{best estimate}}$, could be attributed to variability in quantum dots. The above analysis therefore suggests that the observed broadening in Ca^{2+}-shock experiment was not due to uncertainties in measurement.

2.3.5 The observed broadening in cold-shock experiment was not due to uncertainties in measurement.

Following a similar line of argument as in the previous section, we calculated the best estimate for temperature shift distribution from cold-shock experiments of live and fixed cells. With

Supporting Information - For Review Only - Not for Publication

$\hat{\sigma}\left(\Delta T_{\text{fixed cell}}^{\text{cold shock}}\right)_{\text{apparent}} = 3.09\ ^{\circ}\text{C}$ and $\hat{\sigma}\left(\Delta T_{\text{live cell}}^{\text{cold shock}}\right)_{\text{apparent}} = 4.48\ ^{\circ}\text{C}$ and the error estimates listed in Table S1, we arrived at $\hat{\sigma}\left(\Delta T_{\text{fixed cell}}^{\text{cold shock}}\right)_{\text{best estimate}} = 1.95\ ^{\circ}\text{C}$ and $\hat{\sigma}\left(\Delta T_{\text{live cell}}^{\text{cold shock}}\right)_{\text{best estimate}} = 3.93\ ^{\circ}\text{C}$ for the distribution widths of fixed and live cells, respectively. The error analysis here therefore suggests that the observed broadening in cold-shock experiment was not due to uncertainties in measurement.

Supporting Information - For Review Only - Not for Publication

Table S1

Uncertainty Source	Characterization Method	Results						
		Expt. Category	# Traj.	# Data Pts.	$\langle\lvert\Delta x\rvert\rangle$[a,b] (pixel)	$\sigma(\lvert\Delta x\rvert)$[c] (pixel)	$\delta(\Delta\lambda)$[d] (nm)	$\delta(\Delta T)$[e] (°C)
Instrument drifts	From Ca^{2+}-shock experiments on fixed-cell Δx statistics	Ca^{2+}-shock fixed cell[f]	45	1895	0.320	0.450	0.0648	0.617
Intracellular QD movements	From quantum dot tracking Δx statistics	Ca^{2+}-shock ($-Ca^{2+}$), $\Delta T > 0$	112	1370	0.413	0.591	0.0852	0.811
		Ca^{2+}-shock ($+Ca^{2+}$), $\Delta T > 0$	112	1717	3.39	1.47	0.212	2.02
		Ca^{2+}-shock ($+Ca^{2+}$), $\Delta T = 0$	51	643	6.95	1.56	0.224	2.14
		Ca^{2+}-shock ($+Ca^{2+}$), $\Delta T < 0$	63	763	4.36	1.85	0.266	2.53
		Cold-shock live	77	2286	3.56	1.48	0.214	2.04
		Cold-shock fixed	56	1462	3.24	1.67	0.241	2.30
						$\sigma(\lvert\Delta x\rvert)$[g] (pixel)	$\langle\delta\hat{\lambda}\rangle$ (nm)	$\delta(\Delta T)$ (°C)
Uncertainties in fitting[g]	From covariance analysis of fitting quantum dot spots[g]	Ca^{2+}-shock fixed	45	1895	-	0.663	0.0955	0.909
		Ca^{2+}-shock ($-Ca^{2+}$), $\Delta T > 0$	112	1370	-	0.393	0.0566	0.539
		Ca^{2+}-shock ($+Ca^{2+}$), $\Delta T > 0$	112	1717	-	0.304	0.0438	0.418
		Ca^{2+}-shock ($+Ca^{2+}$), $\Delta T = 0$	51	643	-	0.376	0.0541	0.515
		Ca^{2+}-shock ($+Ca^{2+}$), $\Delta T < 0$	63	763	-	0.323	0.0465	0.443
		Cold-shock live	77	2286	-	0.226	0.0325	0.310
		Cold-shock fixed	56	1462	-	0.208	0.0300	0.286

[a] The pixel size is 16 mm.
[b] The position shift, Δx, along a given trajectory was calculated relative to the mean position of the first 10 sec of the trajectory.
[c] The standard deviation of the spectrum shift in terms of camera pixels after taking into consideration of slid width confinement.
[d] Wavelength readout uncertainties calculated from the standard deviation of the position shift using a linear dispersion of 9 nm/mm and 0.144 nm/pixel.

Supporting Information - For Review Only - Not for Publication

[e] Temperature measurement uncertainties using wavelength readout uncertainties. The conversion factor was 0.105 nm/°C(*10*).
[f] Ca^{2+}-shock experiments on fixed cell were used to estimate uncertainties due to instrument drift.
[g] Uncertainties from fitting the spectral peak positions, $\delta\hat{y}_{i,t}$.

Supporting Information - For Review Only - Not for Publication

3 DISCUSSION

3.1 Addition of quantum dots did not alter thermal characteristics of a cell.

Here we evaluate whether addition of quantum dot probes to a cell changes the thermal characteristics of the cell. The quantum dot fluorescence images suggested that the area fraction of quantum dot in cells was 3% – 8%, likely due to cell-to-cell physiological variations as well as the loading concentration of quantum dots. To evaluate the potential influence of quantum dot-addition to temperature measurement, we calculated the thermal mass of quantum dots in order to estimate the heat capacity of the quantum dots. The thermal mass per unit volume was calculated using $C = \rho C_P$, where ρ was density (kg m^{-3}), and C_P the specific heat (J kg^{-1}K^{-1}). For CdSe (*30*), $\rho = 5674$ kg m^{-3}, and $C_P = 255$ J kg^{-1}K^{-1} at 300 K, where K is temperature in Kelvin. The property of cytoplasm was approximated by that of water(*30*), for which $\rho = 996.6$ kg m^{-3}, and $C_P = 4180.6$ J kg^{-1}K^{-1}. The ratio of thermal mass of CdSe quantum dots to cytoplasm was estimated to be 1:2.88. Therefore, when adding 5% volume ratio of quantum dots to a cell, for instance, the thermal mass increases only by a factor of 1.7%. Therefore, the addition of quantum dots did not interfere with the manner in which cells store heat.

To evaluate the potential impact of heat transfer by quantum dots, we calculated the thermal diffusivity, $D_{\text{thermal}} = \kappa / \rho C_P$ with κ being thermal conductivity, for the quantum dot nano-thermometer and compared it with that of cytosol. The thermal conductivity(*30*) of CdSe was about 9 W m^{-1} K^{-1} and that of water was 0.61 W m^{-1} K^{-1}. The thermal diffusivity of quantum dots was therefore estimated to be 6.2×10^{-6} m^2 s^{-1} whereas that of water/cytosol was about 1.46×10^{-7} m^2 s^{-1}. That is, the thermal diffusivity of quantum dots was approximately twice as large as that of water. This, together with the small volume of quantum dots, ensured rapid temperature equilibrium with quantum dots' local environment. Finally, in the unlikely event that the CdSe quantum dots formed a straight line, for example, the heat transfer between them would be close to the heat transfer in cytosol. Therefore, quantum dots should not considerably affect the cellular temperature distribution.

3.2 The experiments measured steady-state sub-cellular temperature.

The time t (in seconds) of heat transport was formulated by $t = x^2 / 2D_{\text{thermal}}$, where x (in meters) was the distance of heat transfer. In a single cell, the time for heat transfer across the cell was calculated to be 3 milliseconds, assumed that the length of the cell was ~30 µm. This indicated that, assuming the passive thermal diffusion was the only means of heat transfer, any temperature differences should reach an equilibrium state or a steady state on the order of milliseconds inside the cell, much faster than the time resolution of the current experimental setup (30 – 100 ms exposure time per frame). Any active heat transfer such as convection would only speed up heat transfer rate. In other words, if living cells responded to the external stimuli and actively generated heat during the experiments, the measured temperature profile should be understood as the quasi-steady state temperature.

3.3 The observed quantum-dot spectral shifts were not due to intracellular pH changes.

In general, the spectroscopic properties of organic dyes tend to be a strong function of pH. This unfavorable characteristic makes it challenging to measure local temperatures inside living cells using standard temperature sensitive organic dyes. On the other hand, because the emission center of the CdSe/ZnS core/shell quantum dots is the CdSe core, it should be shielded from the chemical environment by the ZnS shell as well by the streptavidin over-coating. Hence, the impact of chemical environment on the quantum dots emission should be relative minor compared to most conventional dyes. To be prudent, we characterized quantum dot emission in intact cells by systematically varying the buffer pH. Cells were incubated at different pH levels in PBS and the spectral shift at room temperature was examined. Before changing the pH levels, cells were washed with PBS three times first and then incubated at fresh buffer solution with different pH. The results, averaged from two sets of independent

Supporting Information - For Review Only - Not for Publication

experiments, are displayed Fig. S7, indicate weak pH dependence under the experimental conditions. Moreover, the apparent temperature shift appears to level out at extreme pH levels; that is, according to this data set, the maximum temperature change caused by intracellular pH change is roughly $\delta(\Delta T) = \pm 1\,^{\circ}\mathrm{C}$. This is much smaller than the observed local temperature change upon Ca^{2+} shock, which could be as high as $\Delta T = +8\,^{\circ}\mathrm{C}$ (cf. Fig. 2d in the main text).

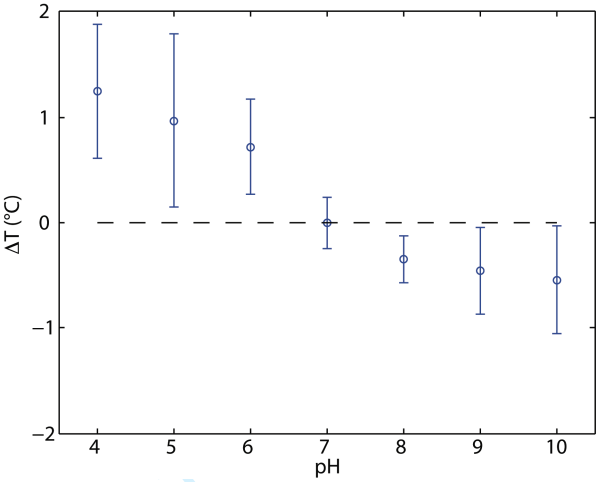

Fig. S7. Apparent temperature as a function of pH, as converted from measured quantum dot spectral shift relative to pH = 7. For each experiment, the spectral shift was calculated relative to the spectral mean across all pH levels. The error bars were one standard deviation and were propagated combining fitting errors and differences from two measurements.

With respect to potential cold-shock induced pH, several studies have shown that the temperature dependence of intracellular pH (*31, 32*) is rather mild. In general, increasing temperature tends to decrease the pH, driving the system to become more acidic. For example, in frog skeletal muscles (*32*), a temperature cooling from 39.4 °C to 4.6 °C results in a pH change from $p\mathrm{H} \sim 6.95$ to $p\mathrm{H} \sim 7.38$. The pH was found to depend linearly on $1/T$ where T is absolute temperature in Kelvin. In the cold shock experiment, the ambient temperature was lowered from 37 °C to 15 °C. Using that set of data, we estimated that the pH change should be within pH = 6.98 (37 °C) and pH = 7.24 (15 °C). Therefore, it is unlikely that the observed spectral shift in quantum dots upon cold shock was due to cooling induced shift in pH.

3.4 Quantum dot spectral shift was independent of the illumination intensity.

We characterized quantum dot emission spectra in intact cells with respect to different illumination lamp power. The average emission peaks remained the same at four different excitation intensities (Fig. S8). The results indicated that the lamp illumination did not contribute to appreciable heating to the quantum dot temperature probes. They also implied that there were no apparent photo-chemical reactions that might adversely impact on the measurements.

Supporting Inform... For Review Only - Not for Publication

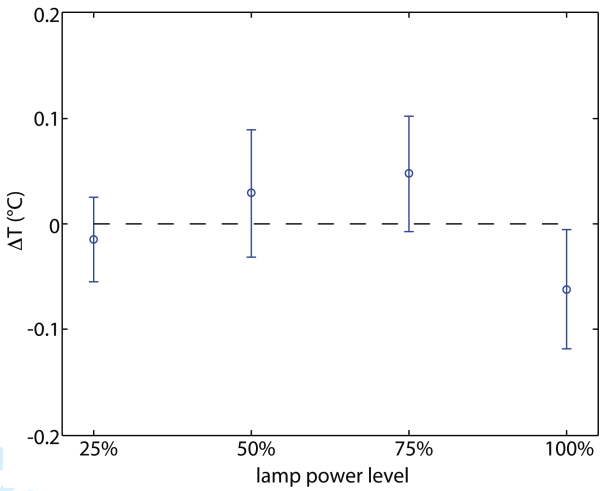

Fig. S8. Quantum dot temperature variations, converted from measured spectral shift, as a function of the illumination lamp power.

3.5 Intra-cellular calcium concentration was increased by addition of solution of ionomycin calcium complex.

To assess the intra-cellular calcium concentration [Ca^{2+}] in Ca^{2+}-shock experiments, we used a fluorescent dye, fluo-4 (Invitrogen / Molecular Probes, F10471) in a separate control experiment. Fluo-4 was chosen because it provided bright fluorescence emission for indicating Ca^{2+} concentration at the range of 100 nM to 1 mM. In the experiment, flou-4 was loaded to cells according to manufacturer's protocol. At 40 second into the experiment, ionomycin calcium solution was added to the sample to raise the extracellular [Ca^{2+}] to 1 µM. The resulting increase in fluorescent emission intensity of fluo-4 is shown in Fig. S9a. The average intensity of fluo-4 as a function of time is displayed in Fig. S9b. This experiment suggested that the calcium concentration was elevated by about a factor of two after introducing ionomycin to the extracellular medium.

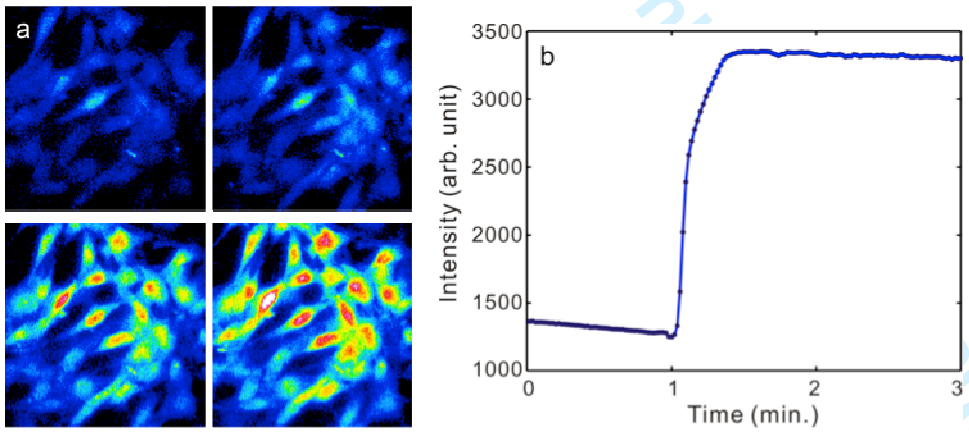

Fig. S9. Fluorescence image of the Fluo-4 calcium indicator. **a.** Snapshots of the fluorescent image at 0, 1, 2, and 3 minutes into the experiment. The intensity is color coded from blue to green to red. **b.** Fluo-4 emission intensity as a function of time.

Supporting Information - For Review Only - Publication

3.6 The majority of the cells remained viable within 20 minutes of cold shock.

We have extensively studied the cellular behavior under cold exposure. It was important to verify that cells were alive during the cold shock experiments. To this end, separate control experiments were carried out to examine cell viability after 10 to 20 minutes of cold exposure. After the cold shock procedure, cell layer was dispersed by 0.25% Trypsin and 0.53-mM EDTA solution. The cell suspension was then stained using 0.4% Trypan blue for 5 minutes at room temperature. The number of viable cells and dead cells was analyzed by counting under a hemocytometer. The viability of the NIH/3T3 cells slightly decreased when cells were exposed to cold environment for a prolonged duration (Fig. S10). Nonetheless, more than 80 % of the cells were deemed viable after 20 minutes of cold shock. We therefore limited our experiment to within 20 min.

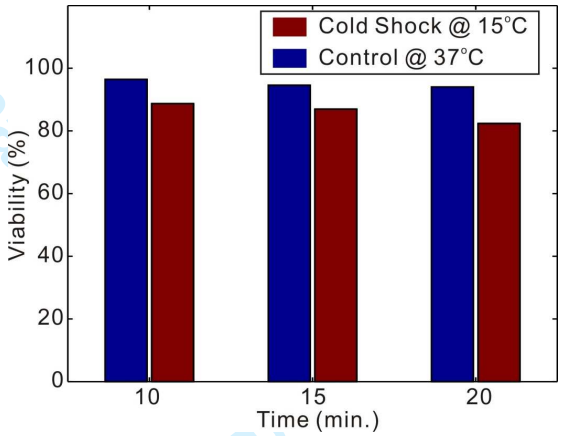

Fig. S10. Statistics of cell viability for the NIH/3T3 cell under different duration of cold exposure at 15 °C.

3.7 The temperature distribution in cold-shock experiment was not due to heat transfer within finite cell thickness.

We performed computational modeling for our system using finite element method (Multiphysics, COMSOL). Using the same published parameters mentioned in section 3.1,The simulation model included the glass bottom Petri dish, culture media, a single cell, and surrounding air (Fig. S11a,b). The material and thermal properties of the cell and the culture media were approximated using those of water. Fig. S11c shows the cooling profiles of the model at two test points, at the top of the cell and at the bottom of the cell, separated by ten micrometers. The first observation one may make is that the cooling profiles appear qualitatively similar to what have been measured by the quantum dot thermometer (cf. Fig. 3b and 3c in the main text). The profiles show that the two test points have exactly the same temperature during cooling process. The simulations suggested that the temperature we measured were not affected by the cell thickness.

Supporting Information
Preview Only - Not for Publication

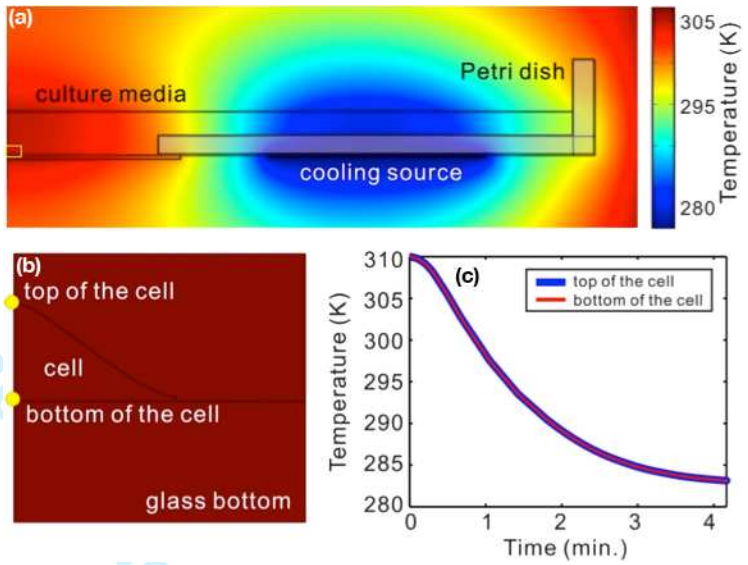

Fig. S11. COMSOL multiphysics simulation of the system under the cold-shock conditions. **a.** The temperature profile of the whole system with one cell, culture media, and Petri dish. **b.** Magnified side-view of the cell in **a**. The filled yellow circles indicate two test points, one at the bottom of the cell closer to the Peltier pad and the other on the top of the cell. **c.** The resulting simulated cooling profile of two different locations of the cell indicated in **b**.

3.8 Estimation of heat released

As emphasized throughout, the current technology could not yet rigorously afford the measurement of absolute temperature. Nevertheless, it would be instructive to estimate the order of magnitude for the heat generated, given the measured temperature change. For this purpose, we assumed without loss of generality the heat to emanate from a three-dimensional Gaussian distribution,

$$q(r) \equiv \frac{q_0}{\sigma_q^3(\sqrt{2\pi})^3} \exp\left[-\frac{r^2}{2\sigma_q^2}\right], \tag{S11}$$

where $q(r)$ the heat released per unit time per unit volume with a unit of $\mathrm{W \cdot m^{-3}}$, q_0 (with unit of W) is the total wattage output of the heat source and σ_q can be understood as the size of the heat source. The heat equation is then (*33*),

$$\frac{\partial}{\partial t}T(r,t) = \frac{\kappa}{C_p\rho}\nabla^2 T(r,t) + \frac{q(r)}{C_p\rho}, \tag{S12}$$

where r is the distance from the heat source center (assuming isotropic medium with spherical symmetry), T is the temperature change in Kelvin, and κ, C_p, and ρ have been defined in section 3.1. Since the experiments measured apparent steady-state temperature changes ($\frac{\partial}{\partial t}T(r,t) \approx 0$, cf. section 3.2), the heat conduction equation reduced to Poisson's equation,

$$\nabla^2 T(r) + \frac{q(r)}{\kappa} = 0. \tag{S13}$$

With the boundary conditions

$$\lim_{r\to\infty} T(r) = T_0,$$

Supporting Information for Review Only. Not for Publication

and

$$\lim_{r\to 0} T(r) = \text{finite},$$

the solution is,

$$T(r) = T_0 + \frac{q_0}{4\pi r\kappa}\,\text{erf}\left[\frac{r}{\sqrt{2}\sigma_q}\right], \tag{S14}$$

where T_0 is the ambient temperature. The temperature difference at the heat source compared to the ambient temperature is therefore,

$$\Delta T = \lim_{r\to 0} T(r) - T_0 = \frac{q_0}{2\sqrt{2}\pi^{3/2}\kappa\sigma_q}. \tag{S15}$$

That is, if the quantum dot nano-thermometer is located at the center of heat source with temperature increase readout of ΔT, the total wattage output for that particular heat source is,

$$q_0 = 2\sqrt{2}\pi^{3/2}\kappa\sigma_q\Delta T. \tag{S16}$$

An immediate consequence of equations (S15) and (S16) is that if the heat source is very localized (confined σ_q), little heat generating power (small q_0) will be sufficient to produce significant and detectable temperature increase ΔT.

The size of the local heat source is unknown at this point, and would be of great interest in future studies. To estimate the heat generated, we considered the intra-cellular volume as projected onto a camera pixel ($16\ \mu\text{m} \times 16\ \mu\text{m}$). With a 20x microscope objective, the pixel size corresponded to a disk in the cell of 400-nm radius. Assuming that the quantum dot nano-thermometer was at the heat source, which had a range of $\sigma_q = 100$ nm in Eq. (S16), and using $\kappa_{\text{water}} = 0.61\ \text{W}\cdot\text{m}^{-1}\cdot\text{K}^{-1}$ (cf. section 3.1) and $\Delta T = +10$ K (an extreme case), one arrived at an estimate for the local heat discharge, $\sim 9.6\ \mu\text{W}$. Similarly, for an average of $\Delta T = +1$ K cellular temperature increase upon Ca^{2+} shock, the average heat released was on the order of ~ 960 nW.

As mentioned earlier (cf. 1.3), mitochondria and Ca^{2+}-ATPases were two likely intra-cellular heat-generating sources. If absolute temperature readout could be reached, one could use the methods discussed by Kjelstrup *et al.*(*34-36*) to provide a more accurate modeling. This, however, is beyond the scope of the current work.

Supporting Information - For Review Only - Not for Publication

4 REFERENCE

1. K. Hanaki *et al.*, *Biochem. Biophys. Res. Commun.* **302**, 496 (Mar, 2003).
2. J. K. Jaiswal, H. Mattoussi, J. M. Mauro, S. M. Simon, *Nat. Biotechnol.* **21**, 47 (Jan, 2003).
3. L. de Meis, *Biosci. Rep.* **21**, 113 (Apr, 2001).
4. L. de Meis, *J. Biol. Chem.* **276**, 25078 (Jul, 2001).
5. L. de Meis, L. A. Ketzer, R. M. da Costa, I. R. de Andrade, M. Benchimol, *PLoS One* **5**, (Mar, 2010).
6. L. de Meis, A. P. Arruda, D. P. Carvalho, *Biosci. Rep.* **25**, 181 (Jun, 2005).
7. G. Inesi, D. Lewis, C. Toyoshima, A. Hirata, L. de Meis, *J. Biol. Chem.* **283**, 1189 (Jan, 2008).
8. M. Suzuki, V. Tseeb, K. Oyama, S. Ishiwata, *Biophys. J.* **92**, L46 (Mar 15, 2007).
9. V. Cusimano, F. Pampinella, E. Giacomello, V. Sorrentino, *Proc. Natl. Acad. Sci. U. S. A.* **106**, 4695 (Mar, 2009).
10. S. Li, K. Zhang, J. M. Yang, L. W. Lin, H. Yang, *Nano Lett.* **7**, 3102 (Oct, 2007).
11. K. Levenberg, *Quart. Appl. Math.* **2**, 164 (1944).
12. D. W. Marquardt, *J. Soc. Indust. Appl. Math.* **11**, 431 (1963).
13. W. H. Press, S. A. Teukolsky, W. T. Vetterling, B. P. Flannery, *Numerical Recipes in C++: The Art of Scientific Computing*. (Cambridge University Press, Cambridge, ed. 2, 2002).
14. C. S. Xu, H. Kim, H. Yang, C. Hayden, *J. Phys. Chem. B* **112**, 5917 (2007).
15. K. Matusita, *Ann. Inst. Stat. Math.* **3**, 17 (1951).
16. K. Matusita, H. Akaike, *Ann. Inst. Stat. Math.* **4**, 11 (1952).
17. K. Matusita, *Ann. Math. Stat.* **26**, 631 (1955).
18. K. Matusita, H. Akaike, *Ann. Inst. Stat. Math.* **7**, 67 (1955).
19. E. Hellinger, *Journal Fur Die Reine Und Angewandte Mathematik* **136**, 210 (1909).
20. K. Matusita, *Ann. Inst. Stat. Math.* **8**, 67 (1956).
21. K. Matusita, *Ann. Inst. Stat. Math.* **16**, 305 (1964).
22. K. Matusita, *Ann. Inst. Stat. Math.* **19**, 181 (1967).
23. K. Matusita, *Ann. Inst. Stat. Math.* **23**, 137 (1971).
24. N. A. Malik, T. Dracos, D. A. Papantoniou, *Exp. Fluids* **15**, 279 (1993).
25. D. N. Li, Y. H. Zhang, Y. G. Sun, W. Yan, *Meas. Sci. Technol.* **19**, (Oct, 2008).
26. B. L. Welch, *Biometrika* **34**, 28 (1947).
27. D. Freedman, P. Diaconis, *Zeitschrift Fur Wahrscheinlichkeitstheorie Und Verwandte Gebiete* **57**, 453 (1981).
28. H. Levene, in *Contributions to Probability and Statistics Essays in Honor of Harold Hotelling,* I. Olkin, Ed. (Standford University Press, Stanford, 1960), pp. 278-292.
29. K. Zhang, H. Chang, A. Fu, A. P. Alivisatos, H. Yang, *Nano Lett.* **6**, 843 (2006).
30. D. R. Lide, W. M. Haynes, Eds., *CRC Handbook of Chemistry and Physics*, (CRC, ed. 90, 2010), 90.
31. P. Aducci, R. Federico, G. Carpinelli, F. Podo, *Planta* **156**, 579 (1982).
32. M. Marjanovic, A. C. Elliott, M. J. Dawson, *J. Membr. Biol.* **161**, 215 (Feb, 1998).
33. H. S. Carslaw, J. C. Jaeger, *Conduction of Heat in Solids*. (Oxford University Press, New York, 1959).
34. S. Kjelstrup, L. de Meis, D. Bedeaux, J. M. Simon, *Eur. Biophys. J. Biophys. Lett.* **38**, 59 (Nov, 2008).
35. S. Kjelstrup, D. Barragan, D. Bedeaux, *Biophy. J.* **96**, 4376 (Jun, 2009).
36. D. Bedeaux, S. Kjelstrup, *Phys. Chem. Chem. Phys.* **10**, 7304 (2008).

Supporting Information - For Review Only - Not for Publication